



OPEN Improved photocatalytic performance of cobalt doped ZnS decorated with graphene nanostructures under ultraviolet and visible light for efficient hydrogen production

Joan J. Kiptarus^{1✉}, Kiptiemoi K. Korir^{1,2,5}, David N. Githinji^{1,3,5} & Henry K. Kiriamiti^{1,4,5}

Highly dispersed Cobalt doped ZnS nanostructures were successfully fabricated on the surfaces of graphene sheets via a simple hydrothermal method. X-ray diffraction (XRD), X-ray photocurrent spectroscopy (XPS), Raman spectroscopy (RS), Fourier transform infrared spectroscopy (FTIR) and Scanning electron microscopy (SEM) were utilized to analyze the structural characteristics of the cobalt doped ZnS decorated with graphene $\text{Co}_x\text{Zn}_{1-x}\text{S}$ rGO nanostructures (NSs). UV-visible optical absorption (UV-vis) studies were conducted to investigate their optical properties. In laboratory studies utilizing water and visible light, the photocatalytic activity of $\text{Co}_x\text{Zn}_{1-x}\text{S}$ rGO NSs at ($x = 0, 1, 2, 4$ and $6 \text{ atm.}\%$) were evaluated. Graphite Oxide (GO) was successfully transformed into sheets of graphene and $\text{Co}_x\text{Zn}_{1-x}\text{S}$ rGO NSs possessed a crystalline structure according to the findings of XRD, RS and FTIR analysis. SEM investigation showed graphene sheets enhanced with ZnS NSs possessed cuboidal, spheroidal form of structure and displayed a paper like appearance. UV-vis confirmed a noticeable rapid increase in transmittance along the UV wavelength area and confirmed a highly transparent NSs in the wavelength range of (180-800 nm). Calculations using density functional theory (DFT) revealed that the Co NSs have more negative conduction bands than ZnS, allowing for effective electron transfer from cobalt to ZnS and exhibiting a band gap decrease as Co content increased. The $\text{Co}_{0.04}\text{Zn}_{0.96}\text{S}$ rGO NSs sample had the highest photocatalytic activity, measured at $7648.9 \mu\text{mol h}^{-1}$. A combination of improved dispersion properties, greater surface area, increased absorption and enhanced transfer of photogenerated electrons, $\text{Co}_x\text{Zn}_{1-x}\text{S}$ rGO NSs increased the photocatalytic hydrogen generation activity.

Keywords Cobalt, Graphene, Hydrogen production, ZnS, Nanostructures, Photocatalytic

There is a need to innovate our energy system by locating green energy resources as a result of the environmental stress on the planet^{1,2}. With over 60% of all global greenhouse gas emissions coming from energy, the United Nations (UN) claims that it is the primary cause of climate change³. As a result, one of the 17 Sustainable Development Goals adopted by the UN also calls for the exploration of new renewable energy sources (Goal 7). Hydrogen is the most abundant and cleanest element in nature^{4,5}, it has the highest energy content in common fuels which is almost three times that of gasoline in the same weight. As an ideal energy carrier, hydrogen can be used in various fields such as, communications and transportation, electric power, architecture and industry⁶. By using a hydrogen-oxygen fuel cell, hydrogen can be converted into electricity and the byproduct of this process is

¹Mechanical, Production and Energy Engineering Department, Moi University, 30100 Eldoret, Kenya. ²Mathematics, Physics and Computing Department, Moi University, 30100 Eldoret, Kenya. ³Manufacturing, Industrial and Textile Engineering Department, Moi University, 30100 Eldoret, Kenya. ⁴Chemical and Processing Engineering Department, Moi University, 30100 Eldoret, Kenya. ⁵These authors contributed equally: Kiptiemoi K. Korir, David N. Githinji and Henry K. Kiriamiti. ✉email: joan.tarus@gmail.com

only water, thus used as a renewable energy. So far, the main ways to obtain hydrogen are by reforming the natural gas, coal, oil, but these approaches usually come along with the emission of carbon dioxides which do not meet the vision of zero carbon emission^{7–9}. Scientists hypothesized that using solar, wind, hydro, geothermal and nuclear energy as power source to produce hydrogen will realize a real zero carbon source of hydrogen production^{10,11}. Future alternatives to fossil fuels that are considered are hydrogen and electric power. However, there remain significant obstacles impeding the growth of hydrogen energy, regardless of how hydrogen is produced, stored, transported, or used⁶. Photocatalytic water splitting is expected to become the dominant method of hydrogen production as a promising approach for clean, economical and environmentally friendly production of hydrogen by using solar energy since Fujishima and Honda first reported the photoelectrochemical water splitting on a TiO_2 electrode in 1972^{12,13}. The relative high energy barrier and slow kinetic properties require utilization of catalyst to improve this situation. At present, noble metal based materials including ruthenium, iridium, rhodium and platinum are the state of the art water splitting electrocatalysts due to their high reactivity in acidic and alkaline condition^{14,15}. However, the cost of using these catalysts on a wide scale is significantly increased by their rarity, mining and refining procedures which have a negative impact on the environment. Exploring a reliable and stable non noble metal based material is therefore the focus of many research efforts⁶. Energy disciplines have been increasingly interested in transition metal base materials such carbides, nitrides, phosphides, sulfides, oxides, and their composites^{16,17}. Transition metal base materials offer a wide range of applications in areas including energy storage and conversion, sensors, and photo or electrocatalysis due to their distinctive electrical structure and great physical properties^{18,19}. Nanostructures materials have become the main attraction for material researchers for the last five decades due to their contributions to different disciplines such as environment, electronics, photonics, medicine, etc. Various kinds of nanomaterials have been developed and are currently utilized in innumerable applications²⁰. Due to their distinctive chemical and electrical structure, ZnS, a group II–VI semiconductor, has attracted a lot of interest because it has proven to be an effective photocatalyst²¹. The large band gap (3.60 eV) prevents it from being utilized for photocatalysis in the visible light range. To fully utilize the potential of sunlight for hydrogen synthesis, a photocatalyst material with visible-light activity must be used^{22–24}. The methods for the synthesis, evaluation, and prospective use of semiconductor and graphene based photocatalysts in photocatalytic hydrogen generation have been examined²⁵. The incorporation of graphene or one of its derivatives into semiconductors significantly improves the photocatalytic performance by improving the adsorption ability, light harvesting in the visible domain and reducing the band gap energy. In the conduction and valence bands, respectively, electrons and holes are produced when semiconductor nanoparticles are subjected to light energy according to their band gap^{26,27}. It has also been studied that such a strategy can prevent the recombination of the photogenerated electron hole pairs^{28,29}. Long lived charge carriers, fewer charge trapping centers, the right energy level offsets and stability against light are all extremely desirable for enhancing the photocatalytic reactivity of a semiconductor photocatalyst³⁰. Despite extensive research on the photocatalytic development studies based on graphene for excellent efficiency of photocatalysts, there are still more research gaps and challenges that need to be extensively examined in the future³¹. This study aims at determining the photocatalytic activity of different hydrothermally produced cobalt doped ZnS decorated with graphene $\text{Co}_x\text{Zn}_{1-x}\text{S}$ rGO nanostructures (NSs) for improved hydrogen production. Scanning electron microscopy (SEM), X-ray diffraction (XRD), X-ray photocurrent spectroscopy (XPS), Fourier Transmission Infra Red Spectroscopy (FTIR) and Raman spectroscopic (RS) microscopy are a few of the methods utilized to describe the surface morphologies and material properties of the nanostructures which were examined using a variety of material parameters including; particle size, crystal structure, surface morphology, chemical composition and band gap. Therefore the investigations of $\text{Co}_x\text{Zn}_{1-x}\text{SrGO}$ NSs photocatalysts are urgently required to validate the photocatalytic efficacy of graphene based semiconductors in the synthesis of hydrogen (H_2) molecules for industrial applications.

Materials and methods

Materials and chemicals

All reagents were of analytical grade and used without any further purification. Zinc acetate, Cobalt acetate and graphite powder were purchased from Alfa Aesar and sigma Aldrich having a purity of 99.999%. Sodium sulfide, sodium sulfite and sodium thiosulfide were provided by Fisher scientific.

Preparation of photocatalysts

GO was prepared from graphite powder by the Hummers method³². In this experiment, ZnS particles were fabricated on the graphene surface via a simple, low cost and easy controllable hydrothermal technique. At the beginning, 60mg of rGO was dispersed in to 50 mL of deionized water (DI) completely by ultrasonication. 440 mg of Zinc acetate dissolved in 15 mL DI was added and suspension heated to 60 °C with magnetic stirring for 2 h. 312 mg of sodium sulfide $\text{Na}_2\text{S}\cdot 9\text{H}_2\text{O}$ dissolved in 15 mL DI was added slowly drop by drop and kept stirring for 4 h for the formation of ZnS NSs on the GO platform. The mixture was then transferred in to a 100 ml Teflon sealed autoclave and heated to 200 °C within 30 min and maintained at this temperature for 16 h and allowed to cool to room temperature naturally. The reaction products were centrifuged for 6 min at 7000 rpm. The reaction precipitate was washed with DI severally to remove unreacted reagents. The washed precipitate was dried in vacuum oven at 60 °C and stored ready for characterization. The same procedure was followed for the synthesis of $\text{Co}_x\text{Zn}_{1-x}\text{SrGO}$ NSs except that varying concentration of $\text{Co}(\text{CH}_3\text{CO}_2)_2\cdot 4\text{H}_2\text{O}$ precursor were combined with $\text{C}_4\text{H}_6\text{Zn}\cdot 2\text{H}_2\text{O}$ precursor during the hydrothermal process.

Characterization techniques

X-ray diffraction was performed by a Bruker D8-Advance diffractometer equipped with graphite monochromatized $\text{Cu K}\alpha$, radiation $\lambda = 0.15405$ nm in the 2θ range from 10° to 80° with a scan rate of 0.08°

per second to determine the crystalline structure of the samples. The experimental spectra were compared to the simulated pattern obtained from the CIF file. The morphology and nanostructure of samples were examined by a (Zeiss Gemini SEM500) Scanning electron microscopy. XPS measurements were carried out using a Thermo K-alpha+ spectrometer using micro focused and monochromated Al K α radiation with an energy of 1486.6 eV. The pass energy for the spectral acquisition was kept at 50 eV for individual core levels. The electron flood gun was utilized for providing charge compensation during data acquisition. Further, the individual core level spectra were checked for charging using C 1s at 284.6 eV as the standard and corrected. The peak fitting of the individual core levels was done using CASAXPS software (CasaXPS Version 2.3.19PR1.0; https://drive.google.com/drive/folders/1TBhxcPSrD66w07gIFuFfywDNiXhr7Z-k?usp=drive_link) with a Shirley-type background. The Phase and chemical identification, molecular structure and their bonding effect was determined using RENISHAW InVia Raman Microscope with Raman shift range (100–4000) cm^{-1} . A Perkin-Elmer Spectrum 100 Fourier-transform infrared (FTIR) spectroscopy was used to study the chemical bonding and molecular structure of the $\text{Co}_x\text{Zn}_{1-x}\text{SrGO}$ NSs. UV-visible optical absorption and transmittance studies of $\text{Co}_x\text{Zn}_{1-x}\text{SrGO}$ NSs were carried out to investigate their optical properties using UV-visible spectrometer (Model: PerkinElmer UV WinLab 6.0.4.0738 / 1.61.00 Lambda 900).

Photocatalytic activity

Photocatalytic water splitting to generate hydrogen was carried out in a quartz photo reactor with a volume of 50 mL. A 430 W Xenon lamp was employed as the side irradiation light source equipped with cutoff filter $\lambda \leq 420\text{nm}$ due to remove UV part. 10 mg of the photocatalyst was dispersed by magnetic stirring in a 50 mL reactor containing 20 mL H_2O solution with addition of 0.1 M Na_2SO_3 and 0.1 M Na_2S mixed sacrificial agent faced to the lamp. Prior to irradiation, the system was deaerated by bubbling high-purity nitrogen for 30 min, then illuminated for 12 h under magnetic stirring. Cobalt doped ZnS with and without graphene were used as a photocatalysts. The top of the Pyrex cell was sealed with a silicone rubber septum. A needle type probe was inserted into the reactor to withdraw generated gas in 120 min intervals. Analyses were conducted on a gas chromatography (Agilent 8890 GC) equipped with a thermal conductivity detector and a 5 Åmstrong molecular sieve packed column. Nitrogen was used as the carrier gas at a flow rate of $30\text{cm}^3\text{min}^{-1}$. The photocatalytic activity of the samples was determined by the quantitatively detected H_2 evolution rate using an external standard in the same concentration range.

Results and discussions

Crystallinity (crystal size and disorder) analysis

The XRD pattern in Fig. 1 shows the crystalline structure and phase of the GO and rGO NSs. Sharp diffraction peaks with no extra signal confirmed the formation of crystalline phase nanostructured material. Functional groups may have been removed from the surface of GO during the thermal treatment to obtain reduced graphene. The absence of significant diffraction peak in the XRD pattern of rGO indicates the exfoliated feature of rGO after the thermal reduction of GO. When GO is reduced to graphene, oxygen may get eliminated and (C–C) bonds change from sp^3 to sp^2 , forming sufficiently on the sheets to offer electronic characteristics.

The Fig. 2 shows powder X-ray diffraction (XRD) patterns of the synthesized $\text{Co}_x\text{Zn}_{1-x}\text{SrGO}$ rGO nanostructures as a function of dopant concentration. The aforementioned patterns exhibit a comparable level of symmetry to the modelled ZnS, ZnO, Co, and CoO database structures. The crystallographic planes (111), (220), and (311) for the hexagonal system are given to the Bragg's peak at $2\theta = 28.25^\circ, 47.84^\circ, 56.93^\circ$ respectively. The attained three XRD peaks are matched well with simulated data files (CIF) which reflected that all the synthesized samples possess the cubic structure of ZnS. The ZnS matrix was successfully filled with Co^{2+} ions, which occupied the

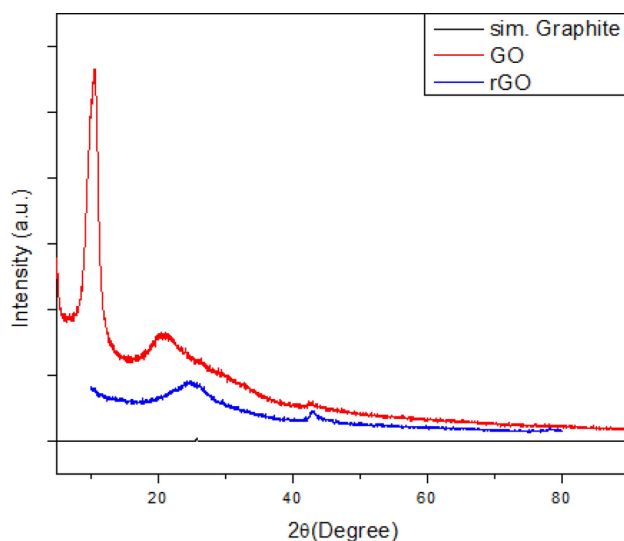


Figure 1. XRD patterns of as-prepared GO-rGO nanostructures.

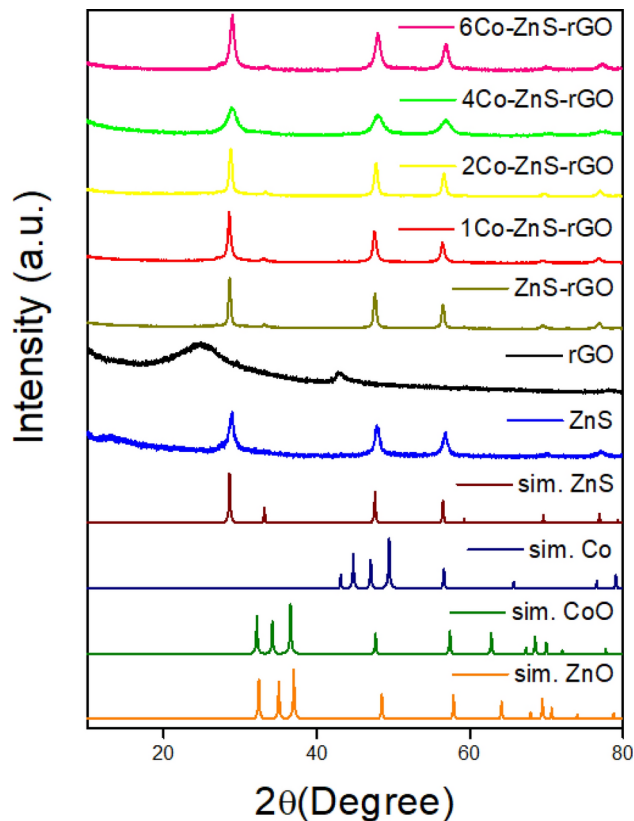


Figure 2. XRD patterns of as-prepared pure Co-ZnS-rGO nanostructures as a function of dopant concentration.

Zn^{2+} sites. The preferred orientation was along (111) plane due to its highest peak intensity throughout the entire samples, identical shift along higher diffraction angles³³. The absence of the typical rGO signal³⁴ in the XRD pattern for (ZnS-rGO) and $Co_xZn_{1-x}S$ rGO NSs could possibly be caused by the formation of zinc sulfide NSs between rGO layers, which would damage the reduced graphite oxide regular layered structure and so the graphene may have been incorporated into the cobalt doped ZnS lattice. The XRD investigation suggested that the doping element cobalt may have been properly substituted into Zn-S lattice, as there were no secondary or impurity phases identified³⁵.

$$D = \frac{K\alpha}{\beta \cos\theta} \quad (1)$$

The peak positions of the cobalt doped samples significantly shift upward in the 2θ values indicates that Co^{2+} (0.58 Å) has a smaller ionic radius compared to that of Zn^{2+} (0.74 Å) in the ZnS^{36,37}. Due to the ionic radius of Cobalt being slightly smaller (0.58 Å) than that of Zn, the peak positions of samples that contain Cobalt exhibit a little shift towards lower 2θ values. The results mentioned above show that the Co^{2+} ions may have been successfully incorporated into the ZnS matrix and occupied the Zn^{2+} sites. On the other hand, it is observed that the replacement of Zn^{2+} ions by Co^{2+} ions result in decrease in intensity of the XRD peaks, which implies that the degree of crystallinity of the samples decreases.

Dopant addition causes changes in the peak intensity and position³⁸. Peak broadening indicates nanocrystal formation in the samples and broadening increases with the substitution of Zn^{2+} ions by Co^{2+} ions. The broadening of the peak may also occur due to micro strains of the crystal structure arising from defects like dislocation, twinning^{39,40}. The broad diffraction peaks were obtained may be due to the small particle effect and this shows that the synthesized samples are in the nano-scale levels. At a low angle, peak broadening is critical for particle size calculation. The average crystalline size was calculated using Debye Scherrer formula^{41,42}. The Full Width at Half Maximum (FWHM) of the XRD peaks for each sample was nearly the same, indicating that the crystallites in the formed NSs are of almost comparable size. The Scherrer equation yielded a crystallite size of (23.5, 18.5, 16.7, 16.2 and 11.1) nm on average for the $Co_xZn_{1-x}S$ rGO nanostructures at ($x = 0, 1, 2, 4, 6$ %) respectively (Supplementary Information Table 1). In comparison to pure ZnS, which has a standard value of 5.406 Å, the values of lattice parameter (a) after doping were at lower levels of (5.394, 5.387, 5.377, 5.75, and 5.354) Å at ($x = 0, 1, 2, 4, 6$ %) (Supplementary Information Table 2). With the exception of the anticipated change in the structure of ZnS caused by cobalt doping, the observed decrease in lattice constant is sufficiently

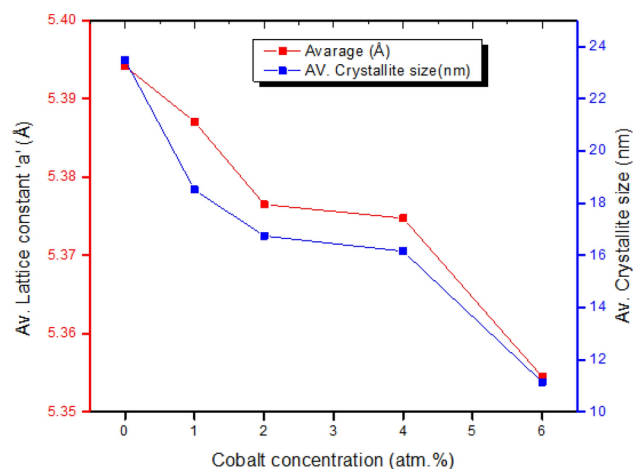


Figure 3. Lattice parameters and crystallite sizes as a function of cobalt concentration.

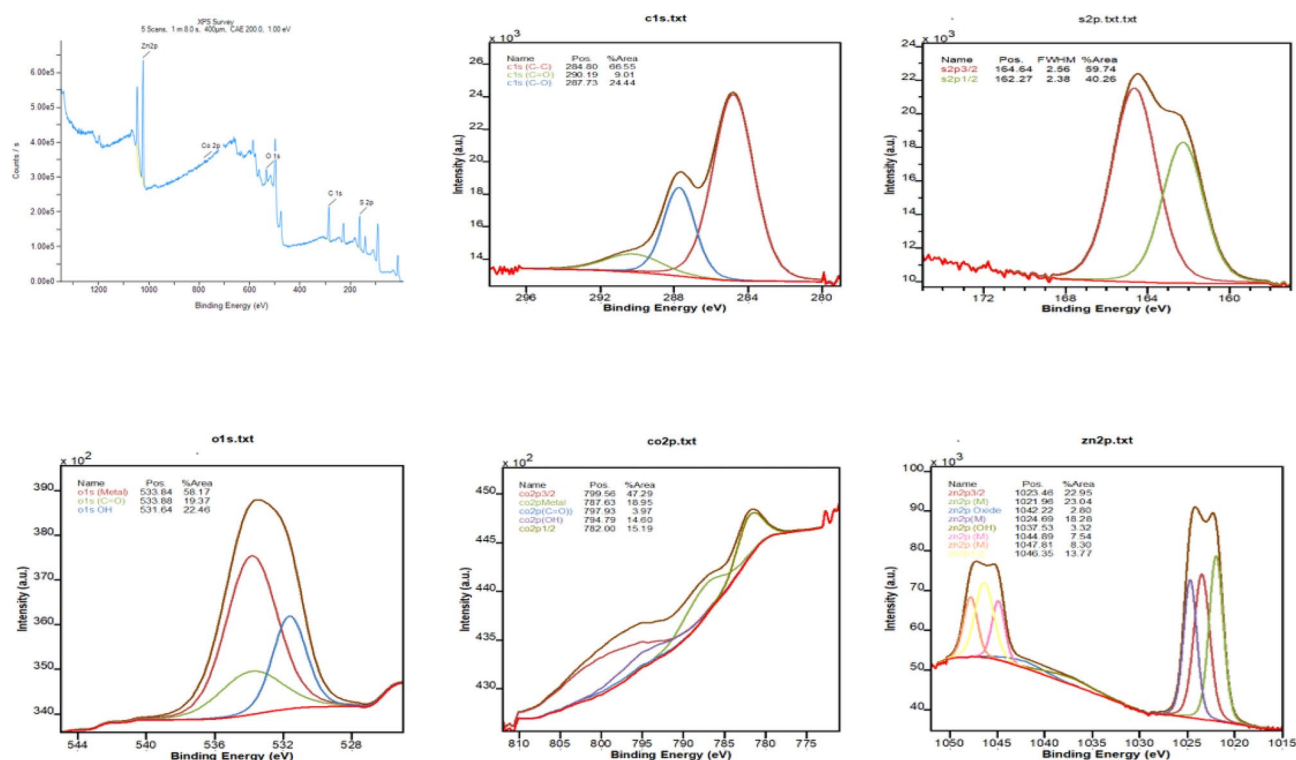


Figure 4. XPS Spectra of pure Co-ZnS-rGO nanostructures.

close to the stated values. Fig. 3 depicts the fluctuation in lattice constant as a function of dopant concentration. The decrease of size was due to the generation of lattice disorder by the cobalt addition as discussed by^{43,44}.

Binding energy analysis

The oxidation states of the elements are further supported by XPS analysis as shown in Fig. 4. In the core level of XPS spectra, the binding energy of $Co_xZn_{1-x}S$ rGO NSs are described. Cobalt doped Zinc sulfide decorated with graphene environments are represented by the Zn, S, C, Co, and O signal peaks in sample Fig. 4 survey at their corresponding standard binding energies. Three Gaussian peaks with centers at 284.8 eV, 290.19 eV and 287.73 eV are displayed for C1s. The peak located at 290.195 eV is attributed to carbon from the C-OH and C=O groups, whereas the peak at 284.8 eV is due to the sp^2 carbon atom. Closely linked to the $O = C - OH$ carboxylic group is the peak at 287.73 eV. The binding energies assigned to the $S2p_{3/2}^3$ and $S2p_{1/2}^3$ are roughly centered at 164.64 eV and 162.27 eV, respectively. This is in good agreement with a previous report on Co_9S_8 crystals⁴⁵. $S2p_{3/2}^3$ and $S2p_{1/2}^3$ oxides are consequently generated at the surface.

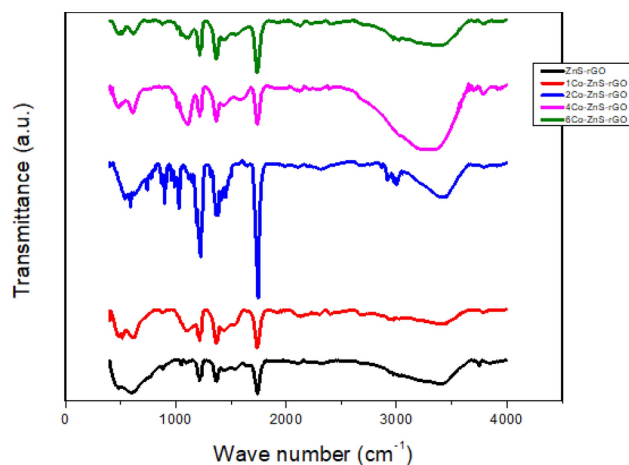


Figure 5. FTIR spectra of Co–ZnS–rGO nanostructures.

The binding energies for $Co2p_{3/2}$ and $Co2p_{1/2}$ are centered at around 799.56 eV and 782 eV, respectively, according to the $Co2p$ XPS spectra at 4% cobalt doping. Peak width is broad to show the presence of more than one Co species such as $Co2p$ (C=O), $Co2p$ (OH) and $Co2p$ metal which shows the presence of cobalt atoms at Co^{2+} state in ZnS lattice. The attribution of the doublets to $Co2p_{3/2}$ and $Co2p_{1/2}$ is in consistency with⁴⁶ findings. The presence of a number of oxygen species is shown by the wide and asymmetric XPS spectra of O1s in Fig. 4. The first O1s is positioned at 531.64 eV which could be made up of intrinsic Oxygen atoms bonded to metals Co and Zn. The second O1s at 533.4 eV could be connected to Carbon double bond and third O1s is connected to adsorbed oxygen at 533.8 eV to form metal hydroxides at the surface. The XPS spectrum of $Zn2p$ shows only a small binding energy shift in the $Zn2p_{3/2}$ region (1021–1024) eV, modal value. Peak width is broad to show the presence of more than one Zn species. However, $Zn2p_{1/2}$ centered at 1046 eV shows a binding energy region (1044–1047) eV due to more than one Zn species hence preserving the spin-orbit split. Two shakeup satellites and three spin-orbit doublets comprised the core level of the $Zn2p$ spectrum. $Zn2p_{3/2}$ and $Zn2p_{1/2}$ are responsible for the first doublet at 1021.96 eV, 1042.22 eV, 1024.69 eV and the second at 1044.89 eV, 1047.81 eV, 1046.35 eV, respectively as also explained by^{47,48}.

Chemical bonding and molecular structure analysis

FTIR is the best technique to examine the chemical bonding and identify the organic group of materials. FTIR spectra confirmed the presence of $Co_xZn_{1-x}S$ rGO nanostructures. The graphene sheets are crucial in helping ZnS nanoparticles develop and distribute on their surface and preventing the sheet's agglomeration⁴⁹.

FTIR analyses of reduced graphene in its purest form and a nanostructure of $Co_xZn_{1-x}S$ rGO in a range of ratios is displayed in Fig. 5. An IR spectrum of reduced graphene oxide reveals large peaks at 3401cm^{-1} , 3422cm^{-1} , 2995cm^{-1} and 3376cm^{-1} which revealed (C–H) bonding. However, the (C=O) functional group was evident at its highest of 1735cm^{-1} in all samples. The peaks corresponding to the oxygen functionalities of GO, such as carbonyl, hydroxyl, carboxyl and epoxy groups may have disappeared upon reduction, whereas some other peaks underwent a substantial shift between 1644cm^{-1} to 820cm^{-1} for the (C–O) stretching vibration due to the strong reduction of the graphene oxide by ascorbic acid (AA). This indicates that (AA) has a good reduction ability^{50,51}. The broad absorption bands for all samples between $1856\text{--}2790\text{cm}^{-1}$ were attributed to (OH) stretching vibration, which denotes the persistence of water absorption on nanostructures surface⁵². The thin and weak absorption band centered around 875cm^{-1} corresponds to the defect states induced by (Co) substitution in (ZnS) lattice⁵³. (Zn–S) stretching vibrations are caused by the strong bands at $1039\text{--}1584\text{cm}^{-1}$ ⁵⁴. The bands that correlate to (Zn–S) exhibit the best degree of concordance with XRD results and previous researches⁵⁵.

Morphological analysis

The surface morphology of the resultant $Co_xZn_{1-x}S$ rGO NSs were characterized using SEM. ZnS doped with cobalt has been tightly and consistently deposited on the surface of the graphene layers as seen in Fig. 6. The images demonstrated that when dopant concentration increases, the size of agglomerations gradually decreases. ZnS NSs largely covered the surface of graphene showing that ZnS exhibited a cuboidal and spheroidal form of structure. The electrical connection between ZnS and graphene sheets may have been made possible by the close contact between the two materials. This might enhance the photocatalytic activity and charge separation of the NSs photocatalysts. SEM Images showed a macro-porous, interconnected, randomly oriented 2D graphene framework with a wrinkled appearance and the dispersion of ZnS nanostructures on the rGO sheets was clearly visible^{56,57}.

The agglomerates on their surface could operate as spacers to successfully avoid the loss of their high active surface area, hence preventing the tightly stacking of graphene sheets. Such a relationship, in conjunction with the excellent mechanical flexibility of graphene sheets, precludes the agglomeration of ZnS NSs, as demonstrated and surface Plasmon allows decreased graphene oxide to absorb light^{58,59}. The properties of reduced graphene

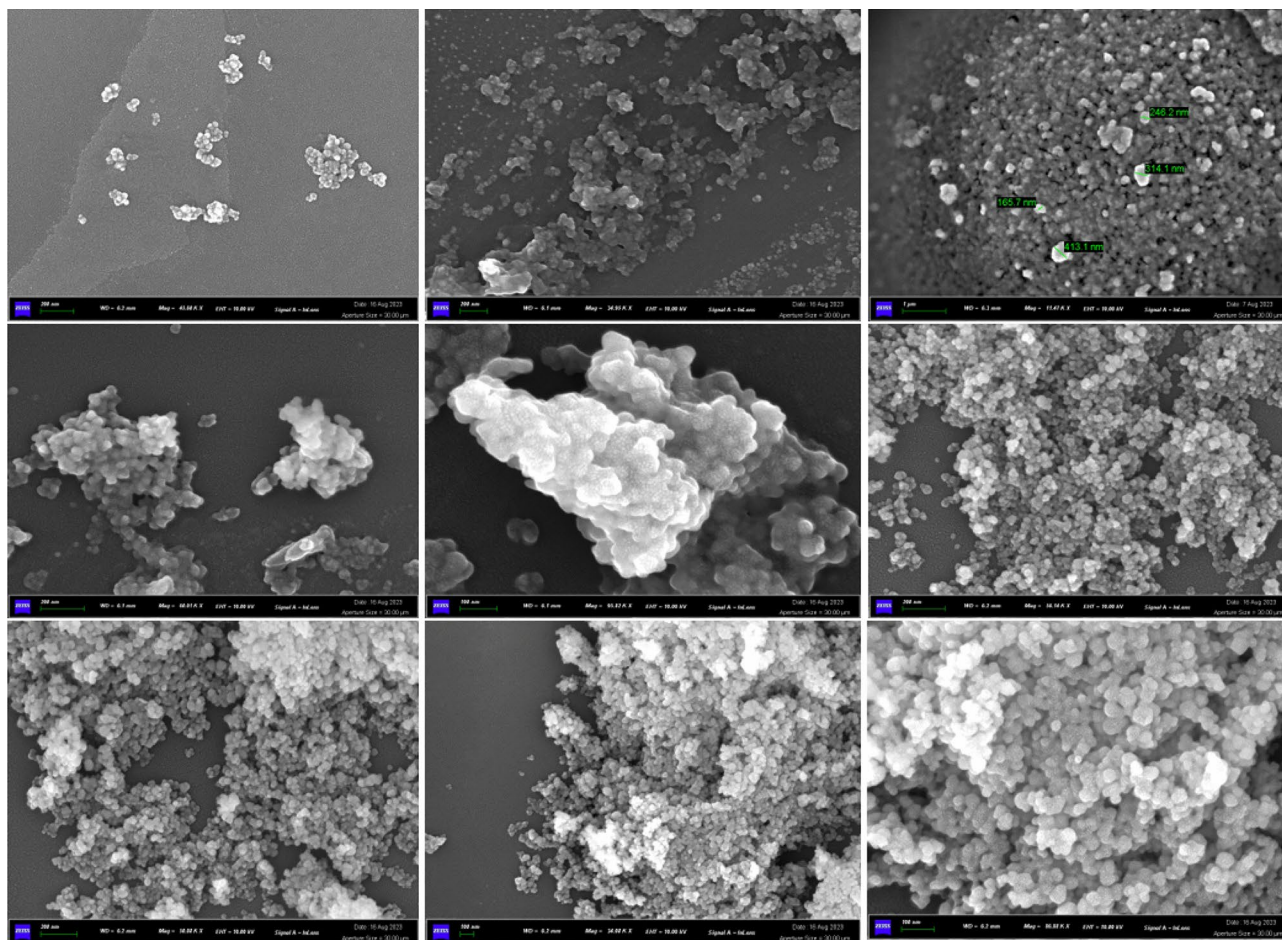


Figure 6. SEM images of pure 4Co-ZnS-rGO nanostructures at different magnification.

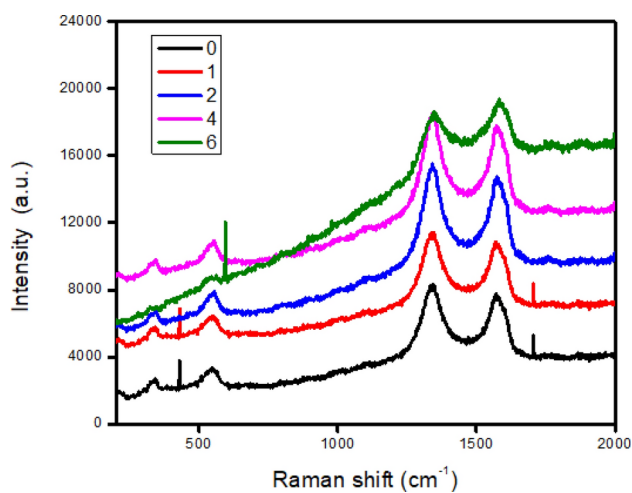


Figure 7. RS spectra of pure Co-ZnS-rGO nanostructures.

include a high electrical conductivity and an adequate capacity for electron storage. The amount of e^- and h^+ recombination may be minimized since graphene may take in and transport excited electrons from ZnS^{60,61}. Therefore, the $Co_xZn_{1-x}S$ rGO may have a higher photocatalytic activity.

Chemical vibration and physical analysis

Raman spectroscopy is commonly used in chemistry to provide a structural fingerprint by which molecules can be identified. Raman spectroscopy identify a material by the Raman shifts and relative intensities of all the Raman bands of the material respectively⁶². A band may shift narrower or broader or vary in intensity, this changes reveals information about stresses in the sample, variation in crystallinity and amount of material respectively⁶³. The frequencies of vibration depend on the masses of the atoms involved and the strength of the bonds between them. Heavy atoms and weak bonds have low Raman shifts^{64,65}.

The Fig. 7 image demonstrates that strong bonds and light atoms exhibit substantial raman shifts. The D and G bands of graphene are represented by the two main, conspicuous bands of GO, which are located at 1341 and 1573 cm^{-1} respectively. Low frequency carbon-carbon (C-C) vibrations are at approximately 650–1233 cm^{-1} , while high frequency carbon hydrogen (C-H) vibrations are found at about 1233–1500 cm^{-1} at (x= 0, 1, 2, 4 and 6 amt.%) in the $Co_xZn_{1-x}S$ rGO NSs spectra. At 1500 – 2000 cm^{-1} , there is additionally a (C=C), (C=O) double bond. Given that hydrogen is lighter than carbon, its vibrations have a greater frequency than carbon's. The spectra also shows the vibrations of two carbon atoms connected by a strong double bond (C=C) at a frequency of about 1706 cm^{-1} . Bond vibration rates are also influenced by the strength of the bond. With the exception of the band at 439 cm^{-1} , which is caused by ZnS spectra light, the bands in the 200–650 cm^{-1} region appear to be caused by the same compounds. The D peak forms as a result of intrinsic structural faults, dangling bonds and disruptions to the symmetric hexagonal graphite lattice⁶⁶. The G band of phonon vibrations in sp^2 bonded carbon materials is linked to the E_{2g} mode. The D band at 1353 cm^{-1} became prominent, suggesting that the sheets may have undergone extensive oxidation and that the sp^2 character had been obliterated. Generally speaking, the intensity ratio of the D and G bands;

$$BandIntensity = \frac{I_d}{I_g} \quad (2)$$

was used to assess the average size and degree of disorder of the sp^2 domains of graphite materials at (x = 0, 1, 2, 4, 6 amt.%). It was deduced that the Eq. (2) ratios of $Co_xZn_{1-x}S$ rGO NSs increased somewhat from (0.84–0.86). This finding suggests that the $Co_xZn_{1-x}S$ rGO NSs may have been doped with additional defects as opposed to fewer GO. This result implies that more defects were doped and GO was reduced in the $Co_xZn_{1-x}S$ rGO NSs.

Absorption and transmittance analysis

The UV absorption spectrum of $Co_xZn_{1-x}S$ rGO at (x = 0, 1, 2, 4, 6%) was observed as shown in Fig. 8. The ZnS characteristic peak corresponding to 3.65 eV band gap is shifted to shorter wavelengths as the size of particle decreased. This blue shift is attributed to the quantum confinement effect at nano scale⁶⁷. The absorption edge of all the samples are well below the visible wavelength i.e., below 400 nm approximately (320–400 nm)⁶⁸.

The two band absorption spectra of the $Co_xZn_{1-x}S$ rGO NSs were discovered to have maxima at 240 and 365 nm, respectively. The bands may match the $\pi - \pi^*$ transition of the aromatic (C–C) and (C=C) bonds as well as the $n - \pi^*$ transition of the carbonyl functional group. The observation of the shift of the NSs absorption peak to a longer wavelength (365 nm) in correlation with the aromatic (C–C) bond's $\pi - \pi^*$ transition implies that GO may have been reduced and the (C–C) bonds restored in the graphene sheets^{69,70}. The UV emission peak

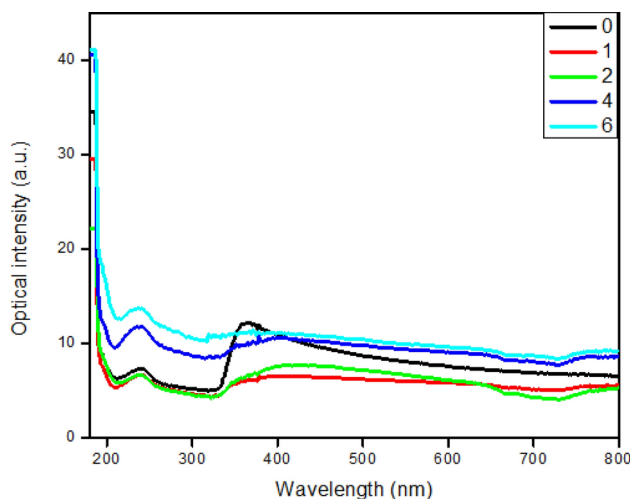


Figure 8. UV absorption spectrum of combined Co–ZnS decorated with graphene.

position gradually shifted from 365 nm to 341 nm. The blue shift of the UV emission peak may have originated from the interaction between the ZnS nanostructures and the graphene sheets⁷¹. The physical mechanism might be attributed to the Burstein Moss effect⁷². Some graphene sheet electrons may have diffused towards the ZnS during the formation of (ZnS-rGO) combinations and collected at the interface between the two materials to form potential barriers. The diffusion of the electrons into ZnS is hampered by the obstacles. These electrons may have resided in the states at the base of ZnS conduction band⁷³. After thermal relaxation, the conduction band's low energy levels may have a sizable population. Both the increase of absorption intensity as well as shift of absorption edge along long wavelength region may be noticed by the substitution of Co into (Zn-S) lattice⁷⁴. The reduced absorption intensity by cobalt addition may be due to the decrease of size and also the proper incorporation of Co^{2+} ions in the position of Zn^{2+} ions where the ionic radius of Co^{2+} ions are lower than that of Zn^{2+} ions consistent with XRD results. The existing shift of absorption edge may have been supported by the size reduction which promote the energy gap to higher value⁷⁵. In addition, the cobalt doping may have stimulated more defects hence created the irregularity or imperfections through (Zn-S) lattice owing to the ionic radius variation which may be a probable reason for the reduction in absorption intensity as demonstrated by⁷⁶. The light scattering by grain boundaries and the reflection of incident light by cobalt clusters in lattice (Zn-S) may have also reduced the absorption intensity^{77,78}.

Photocatalytic activity

Photocatalytic hydrogen production performances of $\text{Co}_x\text{Zn}_{1-x}\text{S}$ photocatalysts prepared with different (Co/Zn) precursor concentration ratios at ($x = 0, 0.01, 0.02, 0.04, 0.06$) with and without graphene decoration for water splitting are shown in Figs. 9a and 10a respectively. The results showed that hydrogen production rates of $\text{Co}_x\text{Zn}_{1-x}\text{S}$ with and without rGO at ($x = 0.04$) cobalt loading recorded the highest photocatalytic hydrogen production mean value after 720 min under UV light irradiation. According to the data presented in Fig. 9a, the hydrogen yield attained at the optimal cobalt loading of ($x = 0.04$) was $3201.562 \mu\text{mol h}^{-1}$, whereas at ($x = 0.06$), the lowest hydrogen yield was $987.432 \mu\text{mol h}^{-1}$ (Supplementary Information Table 3). Additionally, as seen in Fig. 10a, the hydrogen generation rates of $\text{Co}_x\text{Zn}_{1-x}\text{S}$ rGO at ($x = 0.04$) recorded a maximum yield of $7648.9 \mu\text{mol h}^{-1}$ and the lowest being 6% at $2398.7 \mu\text{mol h}^{-1}$ (Supplementary Information Table 4). This demonstrated that, under UV light irradiation, the photocatalytic reaction reached equilibrium after 720 min. Photo-catalyst with the largest surface area showed the highest hydrogen production efficiency.

All the $\text{Co}_x\text{Zn}_{1-x}\text{S}$ rGO samples showed the highest mean value than for $\text{Co}_x\text{Zn}_{1-x}\text{S}$ as demonstrated in Figs. 9b and 10b which describes the error bars for cobalt doped ZnS without and with graphene. The data mean error bars are presented in the column in Figs. 9b and 10b respectively, which also depict the data distribution. It is conclusively shown statistically that the maximum mean value of the hydrogen evolution rate occurs at a concentration of 4%. As can be seen in Fig. 9b, there are no appreciable differences across the data sets since the mean hydrogen evolution response for each sample group overlaps.

The height of each column in the Fig. 10b represents the mean hydrogen generation of cobalt doped ZnS decorated with graphene. According to the graph, the concentration of 4% contributes the largest amount to the evolution of hydrogen, while the concentration of 6% contributes the least. This could be explained by an overabundance of dopant, which results in lower absorption at the visible spectrum hence less evolution of hydrogen^{79,80}.

The current overlapping of error bars in these two figures indicates that concentration did not cause any significant difference in hydrogen evolution and variability in the data can be attributed to systemic and random errors.

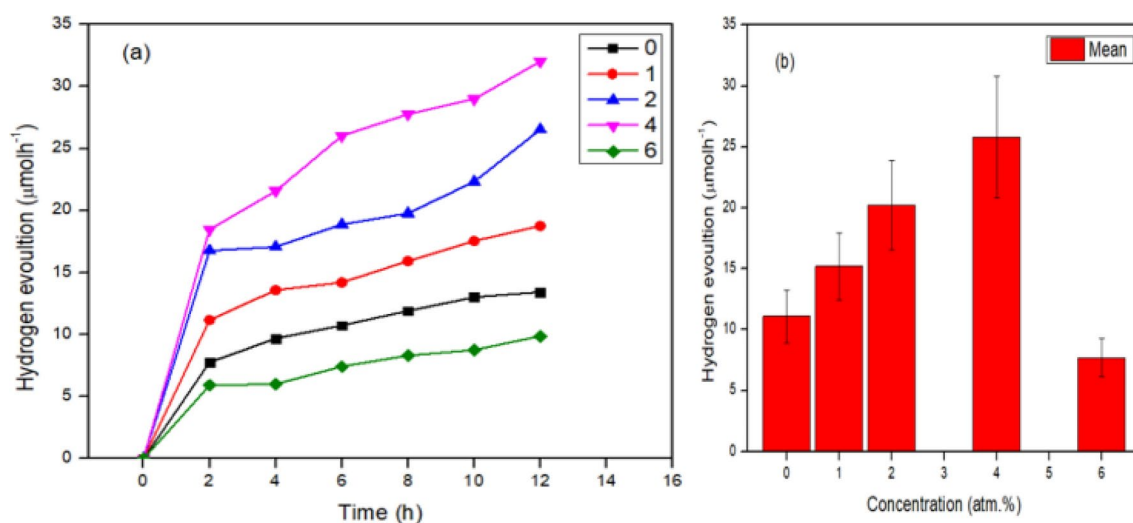


Figure 9. Variation of hydrogen production from pure cobalt doped ZnS NSs without graphene (a) treatment time, (b) concentration of cobalt; The error bars represent plus or minus one standard error of the mean.

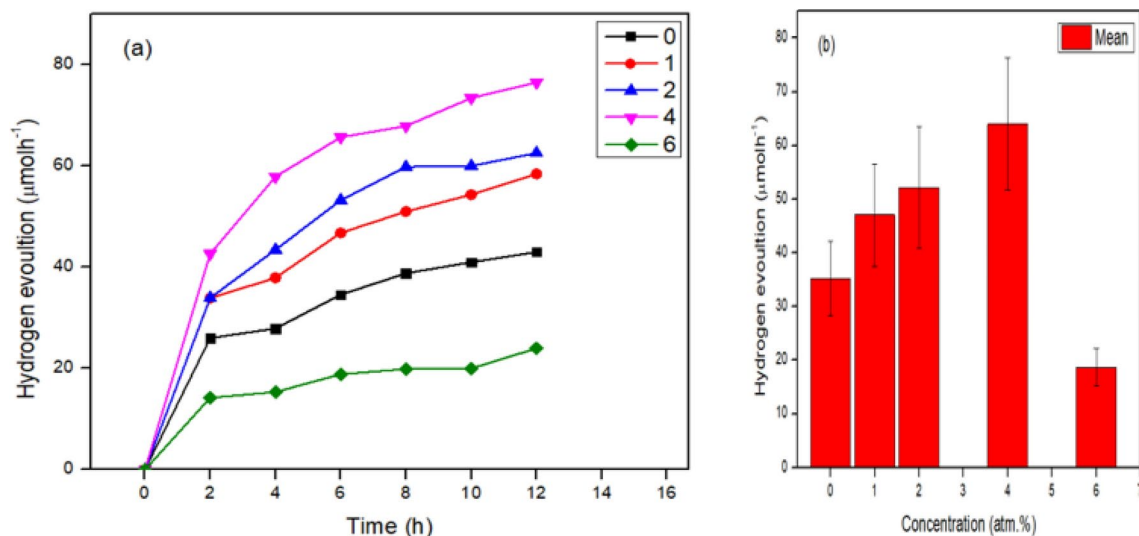


Figure 10. Variation of hydrogen production from pure cobalt doped ZnS NSs decorated with graphene (a) treatment time, (b) concentration of cobalt; The error bars represent plus or minus one standard error of the mean.

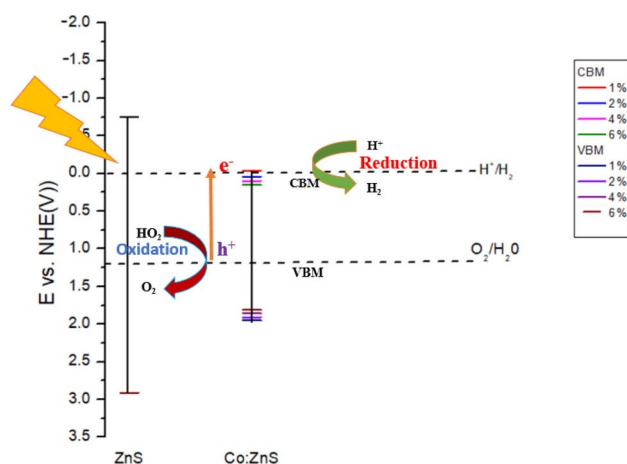


Figure 11. A schematic representation of the photo-generated charge carriers transfer channels and photocatalytic H_2 development for cobalt doped ZnS decorated with graphene.

Proposed mechanism for cobalt doped ZnS decorated with graphene

To further understanding of how photo-generated charge carriers separate in Co, band structure computational study was performed^{81,82}. The improved ZnS's photocatalytic activity was revealed by the use of cobalt doped ZnS band edge alignment computations. Normal hydrogen electrode (NHE), valence band maximal potential (VBM), and conduction band maximum (CBM) have been presented as a result of these analyses^{83,84}. According to density functional theory (DFT) calculations (Supplementary Information Table 5), the maximum position of cobalt conduction band at various concentrations is more negative than the reduction potential of H^+/H_2 (0.0 V vs. normal hydrogen electrode (NHE) at pH 0), suggesting that Co can be used for photocatalytic water splitting for H_2 evolution. A charge transfer channel was predicted at the interface between Co and ZnS under visible light irradiation since, as Fig. 11 demonstrates that the Co NSs have more negative conduction bands than ZnS, which permits efficient electron migration from cobalt to ZnS.

With the suggested mechanism referring to Fig. 12, electrons (e^-) may be triggered from the valence band to the conduction band and migrate to the graphene sheets whenever the ZnS graphene photo-catalyst is subjected to light. Graphene electronic conductivity makes it a useful medium for transporting electrons generated by photons from ZnS's surface to graphene. Hydrogen can be created via the combination of the adsorbed (H^+) ions and electrons. Notably photocatalysts can exhibit a high degree of activity because photocatalytic hydrogen generating processes may occur over a larger reaction area, such as the ZnS surfaces and graphene layer⁸⁵. A similar process that enables charge transfer, separation, and photocatalytic hydrogen production in the reduced graphene oxide $\text{Zn}_x\text{Cd}_{1-x}\text{S}$ system was proposed by^{27,86}. While⁸⁷ investigated the effects of interfacial contact on

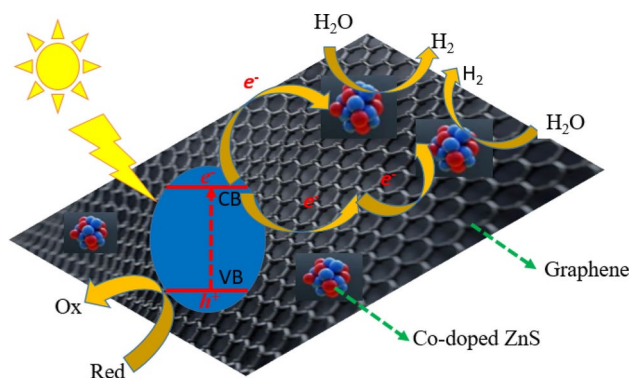


Figure 12. The proposed photocatalytic mechanism for cobalt doped ZnS decorated with Graphene.

the characteristics of α -Fe₂O₃@ rGO nanocomposite and their enhanced solar light photocatalysis,⁸⁸ proposed nickel doped ZnS festooned graphene composites. Furthermore, an improved visible light photocatalytic activity of ZnS/S-graphene quantum dots reinforced with Ag_2S nanoparticles for optical degradation was reported by⁸⁹. A three-dimensional graphene-based photocatalyst was also proposed by⁹⁰; this catalyst's structure may improve charge transfer, increase light adsorption, and broaden the accessible active surface, all of which could raise photocatalytic efficiency.

Conclusions

Different $Co_xZn_{1-x}S$ rGO photocatalysts and visible light active ZnS-rGO NSs were fabricated utilizing a simple hydrothermal method. According to XRD studies, the samples were crystalline and predominantly composed of cubic ZnS phase. The band gaps were greatly reduced, as demonstrated by the blue shift that appears at the ZnS absorption edge resulting from rGO and Co doping, as observed in the UV-visible spectra. The $Co_{0.04}Zn_{0.96}S$ rGO NSs sample exhibited the highest photocatalytic activity while $Co_{0.06}Zn_{0.94}S$ rGO showed the least efficient hydrogen activity. Based on DFT investigations, Co can be employed for photocatalytic water splitting for H₂ evolution since the maximum location of its conduction band at different concentrations is significantly negative than the reduction potential of H⁺/H₂. The experimental results confirm the importance of controlling cobalt doping and show that adding graphene to the nanostructures greatly reduced the rate of electron-hole recombination. Cobalt and rGO's favorable interaction within the nanostructures reduced band gaps, improving hydrogen production. Its development, analysis, and hydrogen evaluation approaches were thoroughly examined, and the results showed that cobalt doped ZnS decorated using graphene is a preferable photocatalyst for hydrogen production.

Data availability

The authors declare that the data supporting the findings of this study are available within the paper and its Supplementary Information files. Should any raw data files be needed in another format they are available from the corresponding author upon reasonable request.

Materials availability

Materials are available from the authors.

Received: 5 April 2024; Accepted: 9 September 2024

Published online: 16 September 2024

References

- Shang, M. *et al.* Understanding the importance of sustainable ecological innovation in reducing carbon emissions: investigating the green energy demand, financial development, natural resource management, industrialisation and urbanisation channels. *Econ. Res.-Ekon. Istraživanja***36**(2) (2023)
- Peter, S. C. Reduction of CO₂ to chemicals and fuels: A solution to global warming and energy crisis. *ACS Energy Lett.***3**(7), 1557–1561 (2018).
- Mai, V. *et al.* The role of robotics in achieving the united nations sustainable development goals-the experts' meeting at the 2021 IEEE/RSJ IROS workshop [industry activities]. *IEEE Robot. Autom. Mag.***29**(1), 92–107 (2022).
- Hassan, Q. *et al.* Renewable energy-to-green hydrogen: A review of main resources routes, processes and evaluation. *Int. J. Hydrogen Energy* (2023).
- Li, X. *et al.* Latest approaches on green hydrogen as a potential source of renewable energy towards sustainable energy: Spotlighting of recent innovations, challenges, and future insights. *Fuel***334**, 126684 (2023).
- Chen, P., Ye, J., Wang, H., Ouyang, L. & Zhu, M. Recent progress of transition metal carbides/nitrides for electrocatalytic water splitting. *J. Alloys Compds.***883**, 160833 (2021).
- Yu, M., Wang, K. & Vredenburg, H. Insights into low-carbon hydrogen production methods: Green, blue and aqua hydrogen. *Int. J. Hydrogen Energy***46**(41), 21261–21273 (2021).
- Bauer, C. *et al.* On the climate impacts of blue hydrogen production. *Sustain. Energy Fuels***6**(1), 66–75 (2022).
- Liu, W., Wan, Y., Xiong, Y. & Gao, P. Green hydrogen standard in china: Standard and evaluation of low-carbon hydrogen, clean hydrogen, and renewable hydrogen. *Int. J. Hydrogen Energy***47**(58), 24584–24591 (2022).

10. Boretti, A. *Supply of Abundant and Low-cost Total Primary Energy to a Growing World Needs Nuclear Energy and Hydrogen Energy Storage* (Elsevier, 2023).
11. Turner, J. A. Sustainable hydrogen production. *Science***305**(5686), 972–974 (2004).
12. Gopinath, C. S. & Nalajala, N. A scalable and thin film approach for solar hydrogen generation: A review on enhanced photocatalytic water splitting. *J. Mater. Chem.* **A9**(3), 1353–1371 (2021).
13. Fujishima, A., Honda, K.: Electrochemical photolysis of water at a semiconductor electrode. *Nature***238**(5358), 37– 38 (1972)
14. Wang, P. *et al.* Highly efficient visible light plasmonic photocatalysts Ag@ Ag (Cl, Br) and Ag@ AgCl-AgI. *ChemCatChem***3**(2), 360–364 (2011).
15. Kiptarus, J. J., Korir, K. K., Githinji, D. N. & Kiriamiti, H. K. A review of design and development of selected transitional metal doped zinc sulphide nanostructure surface layers decorated with graphene for hydrogen production. *Int. J. Mater. Eng.* **14**(1), 12–24 (2024).
16. Wang, X.-T., Ouyang, T., Wang, L., Zhong, J.-H. & Liu, Z.-Q. Surface reorganization on electrochemically-induced Zn–Ni–Co spinel oxides for enhanced oxygen electrocatalysis. *Angew. Chem.* **132**(16), 6554–6561 (2020).
17. Zhao, X., Xue, Z., Chen, W., Wang, Y. & Mu, T. Eutectic synthesis of high-entropy metal phosphides for electrocatalytic water splitting. *ChemSusChem***13**(8), 2038–2042 (2020).
18. Wang, Q., Lai, J. & Sun, D. Review of photo response in semiconductor transition metal dichalcogenides based photosensitive devices. *Opt. Mater. Exp.* **6**(7), 2313–2327 (2016).
19. Patel, R. *et al.* Transition-metal-based layered double hydroxides tailored for energy conversion and storage. *J. Mater. Chem.* **A6**(1), 12–29 (2018).
20. Razali, M.H. & Ismail, N.A. Basic concepts and processing of nanostructures materials. In *Nanoscale Process.* 1– 32 (Elsevier, 2021).
21. Agorku, E. S., Mamo, M. A., Mamba, B. B., Pandey, A. C. & Mishra, A. K. Cobalt-doped ZnS-reduced graphene oxide nanocomposite as an advanced photocatalytic material. *J. Porous Mater.* **22**, 47–56 (2015).
22. Kurnia, F. *et al.* ZnS thin films for visible-light active photoelectrodes: Effect of film morphology and crystal structure. *Crystal Growth Des.* **16**(5), 2461–2465 (2016).
23. Wang, L. *et al.* Anchoring black phosphorus nanoparticles onto ZnS porous nanosheets: efficient photocatalyst design and charge carrier dynamics. *ACS Appl. Mater. Interfaces***12**(7), 8157–8167 (2020).
24. Villa, K., Galán-Mascarós, J. R., López, N. & Palomares, E. Photocatalytic water splitting: Advantages and challenges. *Sustain. Energy Fuels***5**(18), 4560–4569 (2021).
25. Xiang, Q. & Yu, J. Graphene-based photocatalysts for hydrogen generation. *J. Phys. Chem. Lett.* **4**(5), 753–759 (2013).
26. Kamat, P. V. Graphene-based nanoassemblies for energy conversion. *J. Phys. Chem. Lett.* **2**(3), 242–251 (2011).
27. Zhang, Y., Zhang, N., Tang, Z.-R. & Xu, Y.-J. Graphene transforms wide band gap ZnS to a visible light photocatalyst. The new role of graphene as a macromolecular photosensitizer. *ACS Nano***6**(11), 9777– 9789 (2012)
28. An, X. & Jimmy, C. Y. Graphene-based photocatalytic composites. *Rsc Adv.* **1**(8), 1426–1434 (2011).
29. Han, L., Wang, P. & Dong, S. Progress in graphene-based photoactive nanocomposites as a promising class of photocatalyst. *Nanoscale***4**(19), 5814–5825 (2012).
30. Xiang, Q., Yu, J. & Jaroniec, M. Graphene-based semiconductor photocatalysts. *Chem. Soc. Rev.* **41**(2), 782–796 (2012).
31. Ahmed, M. A. & Mohamed, A. A. Recent progress in semiconductor/graphene photocatalysts: synthesis, photocatalytic applications, and challenges. *RSC Adv.* **13**(1), 421–439 (2023).
32. Hummers, W. S. Jr. & Offeman, R. E. Preparation of graphitic oxide. *J. Am. Chem. Soc.* **80**(6), 1339–1339 (1958).
33. Shaili, H. *et al.* Structural, electronic and optical properties of Cu-doped ZnS thin films deposited by the ultrasonic spray method-DFT study. *Opt. Quantum Electron.* **53**(6), 300 (2021)
34. Albers, R. F., Bini, R. A., Souza, J. B. Jr., Machado, D. T. & Varanda, L. C. A general one-pot synthetic strategy to reduced graphene oxide (rgo) and rgo-nanoparticle hybrid materials. *Carbon***143**, 73–84 (2019).
35. Patel, K., Deshpande, M. & Chaki, S. Doping-induced changes in the structural, optical, magnetic and thermal properties of Ni: ZnS nanoparticles prepared by microwave-assisted chemical method. *Appl. Phys.* **A127**, 1–8 (2021).
36. Zaware, R. V., Borse, R. Y. & Wagh, B. G. Properties of thin ZnS: Mn films sprayed by improved method: the role of mn2+ ion concentration. *Mater. Sci. Poland***35**(2), 291–302 (2017).
37. Gurugubelli, T.R., Ravikumar, R. & Koutavarapu, R. Structural, optical, and luminescence properties of Ni 2+-doped ZnO–CdS nanocomposite: Synthesis and investigations for green light emission. *Chem. Pap.* 1–10 (2022)
38. Shakil, M. R. *et al.* Single-doped and multidoped transition-metal (Mn, Fe, Co, and Ni) ZnO and their electrocatalytic activities for oxygen reduction reaction. *Inorgan. Chem.* **57**(16), 9977–9987 (2018).
39. Rehman, A.U. *et al.* Evaluation of spectral, optoelectrical, dielectric, magnetic, and morphological properties of Re3+ (la3+, and Ce3+) and CO2+ CO-doped Zn0.75Cu0.25Fe2O4 ferrites. *Mater. Chem. Phys.* **275**, 125301 (2022).
40. Abu-Elsaad, N., Nawara, A. & Mazen, S. Synthesis, structural characterization, and magnetic properties of Ni–Zn nanoferrites substituted with different metal ions (Mn2+, Co2+, and Cu2+). *J. Phys. Chem. Solids***146**, 109620 (2020).
41. Basak, M., Rahman, M. L., Ahmed, M. F., Biswas, B. & Sharmin, N. The use of X-ray diffraction peak profile analysis to determine the structural parameters of cobalt ferrite nanoparticles using Debye–Scherrer, Williamson–Hall, Halder–Wagner and size-strain plot: Different precipitating agent approach. *J. Alloys Compds.* **895**, 162694 (2022).
42. Fatimah, S., Ragadhita, R., Al Husaeni, D.F. & Nandiyanto, A.B.D. How to calculate crystallite size from X-ray diffraction (XRD) using Scherrer method. *ASEAN J. Sci. Eng.* **2**(1), 65– 76 (2022)
43. Akhtar, M. S. *et al.* Structural, optical, magnetic and half-metallic studies of cobalt doped ZnS thin films deposited via chemical bath deposition. *J. Mater. Chem.* **C3**(26), 6755–6763 (2015).
44. Hamdy, M. S. *et al.* Novel Mg@ ZnO nanoparticles synthesized by facile one-step combustion route for anti-microbial, cytotoxicity and photocatalysis applications. *J. Nanostruct. Chem.* **11**, 147–163 (2021).
45. Greczynski, G. & Hultman, L. X-ray photoelectron spectroscopy: Towards reliable binding energy referencing. *Prog. Mater. Sci.* **107**, 100591 (2020).
46. Major, G.H. *et al.* Perspective on improving the quality of surface and material data analysis in the scientific literature with a focus on X-ray photoelectron spectroscopy (XPS). *J. Vac. Sci. Technol.* **A41**(3) (2023)
47. Chan, M. K. & Ceder, G. Efficient band gap prediction for solids. *Phys. Rev. Lett.* **105**(19), 196403 (2010).
48. Leube, B. T. *et al.* Activation of anionic redox in d0 transition metal chalcogenides by anion doping. *Nat. Commun.* **12**(1), 5485 (2021).
49. Thakre, K. G., Barai, D. P. & Bhanvase, B. A. A review of graphene-TiO2 and graphene-ZnO nanocomposite photocatalysts for wastewater treatment. *Water Environ. Res.* **93**(11), 2414–2460 (2021).
50. Reddy, D. A., Ma, R., Choi, M. Y. & Kim, T. K. Reduced graphene oxide wrapped ZnS–Ag2S ternary composites synthesized via hydrothermal method: Applications in photocatalyst degradation of organic pollutants. *Appl. Surf. Sci.* **324**, 725–735 (2015).
51. Smirnoff, N. Ascorbic acid metabolism and functions: A comparison of plants and mammals. *Free Radic. Biol. Med.* **122**, 116–129 (2018).
52. Kuppayee, M., Nachiyar, G. V. & Ramasamy, V. Enhanced photoluminescence properties of ZnS: Cu2+ nanoparticles using PMMA and CTAB surfactants. *Mater. Sci. Semiconduct. Process.* **15**(2), 136–144 (2012).
53. Pandey, T., Singh, A., Kaundal, R.S. & Pandey, V. Cation exchange doping by transition and non-transition metals: Embracing luminescence to band gap tunability in ZnS lattice. *New J. Chem.* (2023).

54. Abimaheshwari, R., Sakthivel, P. & Vijayasundaram, S. Structural and optical investigations of ZnS quantum dots: Influence of pH value. *Indian J. Phys.* **96**(13), 3755–3760 (2022).
55. Moon, H. *et al.* Design and selective photocatalytic activity of highly concentrated C, N, O CO-doped Zn, S co-defective ZnS particles mediated by ethylenediamine derivatives. *Nano Today* **49**, 101785 (2023).
56. Kiptarus, J.J., Korir, K.K., Githinji, D.N. & Kiriamiti, H.K. Improved photocatalytic performance of cobalt doped ZnS decorated with graphene nanostructures under UV-visible light: Towards efficient H₂ production (2023).
57. Manjunatha, C., Rastogi, C.K., Manmadha Rao, B., Girish Kumar, S., Varun, S., Raitani, K., Maurya, G., Karthik, B., Swathi, C., Sadrzadeh, M. *et al.* Advances in hierarchical inorganic nanostructures for efficient solar energy harvesting systems. *ChemSusChem* **202301755** (2024)
58. Zou, T., Zhao, B., Xin, W., Wang, Y., Wang, B., Zheng, X., Xie, H., Zhang, Z., Yang, J. & Guo, C. High-speed femtosecond laser plasmonic lithography and reduction of graphene oxide for anisotropic photoresponse. *Light Sci. Appl.* **9**(1), 69 (2020)
59. Sajeev, V. *et al.* Terahertz sensing of reduced graphene oxide nanosheets using sub-wavelength dipole cavities. *Sci. Rep.* **13**(1), 12374 (2023).
60. Hu, Y. *et al.* Recent advance of graphene/semiconductor composite nanocatalysts: Synthesis, mechanism, applications and perspectives. *Chem. Eng. J.* **414**, 128795 (2021).
61. Zheng, L., Teng, F., Ye, X., Zheng, H. & Fang, X. Photo/electrochemical applications of metal sulfide/TiO₂ heterostructures. *Adv. Energy Mater.* **10**(1), 1902355 (2020).
62. Smith, E. & Dent, G. *Modern Raman Spectroscopy: A Practical Approach*. (Wiley, 2019).
63. Vandenabeele, P. *Practical Raman Spectroscopy: An Introduction* (Wiley, 2013).
64. McCreery, R.L. *Raman Spectroscopy for Chemical Analysis*. (Wiley, 2005).
65. Campanella, B., Palleschi, V. & Legnaioli, S. Introduction to vibrational spectroscopies. *ChemTexts* **7**, 1–21 (2021).
66. Bhatt, M. D., Kim, H. & Kim, G. Various defects in graphene: A review. *RSC Adv.* **12**(33), 21520–21547 (2022).
67. Ahmed, T. & Edvinsson, T. Optical quantum confinement in ultrasmall ZnO and the effect of size on their photocatalytic activity. *J. Phys. Chem. C* **124**(11), 6395–6404 (2020).
68. Ebrahimi, S., Yarmand, B. & Naderi, N. High-performance UV-B detectors based on Mn_xZn_{1-x}S thin films modified by bandgap engineering. *Sens. Actuators A Phys.* **303**, 111832 (2020).
69. Zhang, Y. *et al.* Facile synthesis of well-dispersed graphene by γ -ray induced reduction of graphene oxide. *J. Mater. Chem.* **22**(26), 13064–13069 (2012).
70. More, M. P. & Deshmukh, P. K. Computational studies and biosensory applications of graphene-based nanomaterials: A state-of-the-art review. *Nanotechnology* **31**(43), 432001 (2020).
71. Bharathi, G. *et al.* Graphene quantum dot solid sheets: Strong blue-light-emitting & photocurrent-producing band-gap-opened nanostructures. *Sci. Rep.* **7**(1), 10850 (2017).
72. Zhou, X. *et al.* Multicolor tunable electrochromic materials based on the Burstein–Moss effect. *Nanomaterials* **13**(10), 1580 (2023).
73. Bao, L. *et al.* Optimizing the electronic structure of ZnS via cobalt surface doping for promoted photocatalytic hydrogen production. *Inorgan. Chem.* **60**(20), 15712–15723 (2021).
74. Heiba, Z. K., Albassam, A. & Mohamed, M. B. Effect of Zn/S non-stoichiometric ratio on the structural, optical and electronic properties of nano-ZnS. *Appl. Phys. A* **126**(6), 479 (2020).
75. Viezbicke, B.D., Patel, S., Davis, B.E., Birnie III, D.P. Evaluation of the Tauc method for optical absorption edge determination: ZnO thin films as a model system. *Phys. Status Solidi (B)* **252**(8), 1700–1710 (2015)
76. Zhu, J. *et al.* Tunable emission of Cu (Mn)-doped ZnInS quantum dots via dopant interaction. *J. Colloid Interface Sci.* **506**, 27–35 (2017).
77. Reddy, D.A., Liu, C., Vijayalakshmi, R. & Reddy, B. Structural, optical and magnetic properties of Zn_{0.97-x}Al_xCr_{0.03}S nanoparticles. *Ceram. Int.* **40**(1), 1279–1288 (2014).
78. Khodabandeh, F., Abdizadeh, H., Avnani, A. A. & Golobostanfard, M. R. Photoelectrochemical water splitting based on chalcopyrite semiconductors: A review. *Int. J. Hydrogen Energy* **65**, 779–803 (2024).
79. Cao, S. & Piao, L. Considerations for a more accurate evaluation method for photocatalytic water splitting. *Angew. Chem. Int. Ed.* **59**(42), 18312–18320 (2020).
80. Chen, S., Takata, T. & Domen, K. Particulate photocatalysts for overall water splitting. *Nat. Rev. Mater.* **2**(10), 1–17 (2017).
81. Zhu, Y. *et al.* A [001]-oriented Hittorf's phosphorus nanorods/polymeric carbon nitride heterostructure for boosting wide-spectrum-responsive photocatalytic hydrogen evolution from pure water. *Angew. Chem. Int. Ed.* **59**(2), 868–873 (2020).
82. Zhu, Y. *et al.* Red phosphorus grafted high-index (116) faceted anatase TiO₂ for z-scheme photocatalytic pure water splitting. *Adv. Funct. Mater.* **34**(9), 2311623 (2024).
83. Wang, Z., Wei, X., Huang, Y., Zhang, J. & Yang, J. High solar-to-hydrogen efficiency in asp/gase heterojunction for photocatalytic water splitting: A dft study. *Materials Science in Semiconductor Processing* **159**, 107393 (2023).
84. Xi, Y. *et al.* Engineering an interfacial facet of s-scheme heterojunction for improved photocatalytic hydrogen evolution by modulating the internal electric field. *ACS Appl. Mater. Interfaces* **13**(33), 39491–39500 (2021).
85. Kumar, S., Kumar, A., Kumar, A. & Krishnan, V. Nanoscale zinc oxide based heterojunctions as visible light active photocatalysts for hydrogen energy and environmental remediation. *Catal. Rev.* **62**(3), 346–405 (2020).
86. Li, Q. *et al.* Enhanced photocatalytic hydrogen-production performance of graphene-ZnxCd_{1-x}S composites by using an organic s source. *Chem. Eur. J.* **20**(4), 1176–1185 (2014).
87. Paulson, E., Jothibas, M. & Srinivasan, S. The effects of interfacial contact on the properties of α -Fe₂O₃@ rgo nanocomposite and their enhanced solar light photocatalysis. *Vacuum* **211**, 111970 (2023).
88. Chang, C.-J., Chu, K.-W., Hsu, M.-H. & Chen, C.-Y. Ni-doped ZnS decorated graphene composites with enhanced photocatalytic hydrogen-production performance. *Int. J. Hydrogen Energy* **40**(42), 14498–14506 (2015).
89. Nekooei, A., Miroliaei, M. R., Nejad, M. S. & Sheibani, H. Enhanced visible-light photocatalytic activity of ZnS/S-graphene quantum dots reinforced with Ag₂S nanoparticles. *Mater. Sci. Eng. B* **284**, 115884 (2022).
90. Shah, N. R. A. M. *et al.* Current progress on 3D graphene-based photocatalysts: From synthesis to photocatalytic hydrogen production. *Int. J. Hydrogen Energy* **46**(14), 9324–9340 (2021).

Acknowledgements

The authors acknowledge the African Development Bank (AFDB), the SAMat Research Facilities, Jawaharlal Nehru Centre for Advanced Scientific Research (JNCASR), Bengaluru, India, Center of Excellence in Phytochemicals, Textile and Renewable Energy (ACE II PTRE) and Moi University, Kenya for support. Thanks Prof. C. N. Rao, Prof. S.C.Peter and Prof. U. Waghmare, JNCASR.

Author contributions

Conceptualization, J.J.K., K.K.K., D.G.N and H.K.K.; methodology, J.J.K. K.K.K and D.G.N software, k.k.k; validation, J.J.K, D.G.N and K.K.K; formal analysis, D.N.G., K.K.K., H.K.K; investigation, J.J.K.; resources, J.J.K., K.K.K.; data curation, K.K.K, D.N.G, H.K.K.; writing—original draft preparation, J.J.K.; writing—review and

editing, J.J.K, K.K.K., D.N.G, H.K.K.; visualization, D.N.G, K.K.K, H.K.K.; supervision, D.N.G, K.K.K, H.K.K.; All authors have read and agreed to the published version of the manuscript.

Declarations

Competing interests

The authors declare no competing interests.

Additional information

Supplementary Information The online version contains supplementary material available at <https://doi.org/10.1038/s41598-024-72645-z>.

Correspondence and requests for materials should be addressed to J.J.K.

Reprints and permissions information is available at www.nature.com/reprints.

Publisher's note Springer Nature remains neutral with regard to jurisdictional claims in published maps and institutional affiliations.

Open Access This article is licensed under a Creative Commons Attribution-NonCommercial-NoDerivatives 4.0 International License, which permits any non-commercial use, sharing, distribution and reproduction in any medium or format, as long as you give appropriate credit to the original author(s) and the source, provide a link to the Creative Commons licence, and indicate if you modified the licensed material. You do not have permission under this licence to share adapted material derived from this article or parts of it. The images or other third party material in this article are included in the article's Creative Commons licence, unless indicated otherwise in a credit line to the material. If material is not included in the article's Creative Commons licence and your intended use is not permitted by statutory regulation or exceeds the permitted use, you will need to obtain permission directly from the copyright holder. To view a copy of this licence, visit <http://creativecommons.org/licenses/by-nc-nd/4.0/>.

© The Author(s) 2024